The Astrophysical Journal, 865:86 (12pp), 2018 October 1 https://doi.org/10.3847/1538-4357/aada12

Investigating the Structure of Vela X

P. Slane[1], I. Lovchinsky[1,2], C. Kolb[3], S. L. Snowden[4], T. Temim[5], J. Blondin[3], F. Bocchino[6], M. Miceli[6], R. A. Chevalier[7], J. P. Hughes[8], D. J. Patnaude[1], and T. Gaetz[1]
[1] Harvard-Smithsonian Center for Astrophysics, 60 Garden Street, Cambridge, MA 02138, USA; slane@cfa.harvard.edu
[2] Department of Physics, Harvard University, USA
[3] North Carolina State University, USA
[4] Laboratory for High Energy Astrophysics, Code 662, NASA/GSFC, Greenbelt, MD 20771, USA
[5] Space Telescope Science Institute, 3700 San Martin Drive, Baltimore, MD 21218, USA
[6] INAF—Osservatorio Astronomico di Palermo, Piazza del Parlamento I, I-90134 Palermo, Italy
[7] Department of Astronomy, University of Virginia, P.O. Box 400325, Charlottesville, VA 22904-4325, USA
[8] Department of Physics and Astronomy, Rutgers University, Piscataway, NJ 08854-8019, USA
Received 2018 July 1; revised 2018 August 2; accepted 2018 August 11; published 2018 September 25

Abstract

Vela X is a prototypical example of a pulsar wind nebula whose morphology and detailed structure have been affected by interaction with the reverse shock of its host supernova remnant. The resulting complex of filamentary structure and mixed-in ejecta embedded in a nebula that is offset from the pulsar provides the best example we have of this middle-age state that characterizes a significant fraction of composite supernova remnants (SNRs), and perhaps all of the large-diameter pulsar wind nebulae (PWNe) seen as TeV sources. Here, we report on an *XMM-Newton* (hereafter *XMM*) Large Project study of Vela X, supplemented by additional *Chandra* observations. Through broad spectral modeling, as well as detailed spectral investigations of discrete emission regions, we confirm previous studies that report evidence for ejecta material within Vela X, and show that equivalent-width variations of O VII and O VIII are consistent with temperature maps within the PWN that show low-temperature regions where the projected SNR emission appears to dominate emission from the ejecta. We identify spectral variations in the nonthermal emission, with hard emission being concentrated near the pulsar. We carry out investigations of the Vela X "cocoon" structure, and with hydrodynamical simulations, show that its overall properties are consistent with structures formed in the late-phase evolution of a composite SNR expanding into a surrounding medium with a density gradient, with ejecta material being swept beyond the pulsar and compressed into an elongated structure in the direction opposite the high external density.

Key words: acceleration of particles – ISM: individual objects (Vela X) – ISM: supernova remnants – shock waves

1. Introduction

Located at a distance of only ~290 pc (Dodson et al. 2003), the Vela supernova remnant (SNR; Figure 1) houses a young pulsar that powers the extended pulsar wind nebula (PWN) Vela X. The PWN extends to the south of the pulsar, apparently the result of an asymmetric reverse shock (RS) interaction associated with a large-scale density anisotropy surrounding the SNR (e.g., Blondin et al. 2001). Observations across the electromagnetic spectrum have been used to characterize the emission properties and overall structure of the PWN, as described below.

Radio observations of the Vela SNR (G263.9−3.3; Milne 1968) show a large (~6° diameter) shell-type remnant with a central flat-spectrum PWN (Vela X). Studies of neutral hydrogen in the Vela direction reveal a thin shell surrounding the SNR, with a density $n_0 \approx 1\,\mathrm{cm}^{-3}$ (Dubner et al. 1998), while X-ray observations of the SNR with the *ROSAT* observatory (Aschenbach et al. 1995) show a limb-brightened shell of thermal X-rays whose brightest emission is in the northeastern hemisphere, toward the Galactic plane. An overall asymmetry of Vela is evident, with the emission in the south/southwest extending to larger radii (Figure 1). Distinct bowshock-like structures are observed along, or just outside, the SNR shell, with subsequent studies confirming that these appear to be high-velocity ejecta fragments that have exited the SNR (e.g., Tsunemi et al. 1999). Bocchino et al. (1999) show that the emission in the northeast (NE) region is characterized by two distinct temperature components ($kT_1 \approx 0.1$ keV, $kT_2 \approx 0.5$ keV), possibly indicating expansion into a surrounding medium with dense clouds and a low-density intercloud medium (ICM; $n_{\rm ICM} \approx 0.01$–$0.1\,\mathrm{cm}^{-3}$). Using *XMM* observations, Miceli et al. (2005) carried out observations of shock-cloud interactions along the northern rim of Vela and concluded that the two distinct temperature components reported in earlier studies are both associated with the clouds, leading to an upper limit $n_{\rm ICM} < 0.06\,\mathrm{cm}^{-3}$. Optical and far-UV studies of Vela "fragment D," located outside the eastern limb, indicate interaction of this ejecta knot with an external cloud with $n_{\rm cl} \approx 4$–$11\,\mathrm{cm}^{-3}$, providing additional evidence for a higher overall density in the northern and western regions of the SNR (Sankrit et al. 2003).

A ^{12}CO survey of molecular clouds (MCs) in the vicinity of the Vela SNR (Moriguchi et al. 2001) establishes the presence of a high MC concentration outside the northern limb of the remnant, but little CO in the west/southwest where the X-ray emission is more extended. This suggests an inhomogeneous density distribution in the pre-explosion environment with an intercloud density $n_{\rm ICM} \approx 0.01\,\mathrm{cm}^{-3}$, similar to that inferred from X-ray studies, although the presence of an HI shell indicates a cooling shock that requires a considerably higher density given the observed SNR radius, illustrating that the medium surrounding the SNR is complex.

The Vela pulsar, located in the central regions of the SNR, has a spin period of 89.3 ms, a characteristic age $\tau_c = 11.3$ kyr, and a spin-down power $\dot{E} = 7 \times 10^{36}\,\mathrm{erg\,s}^{-1}$. *Chandra*

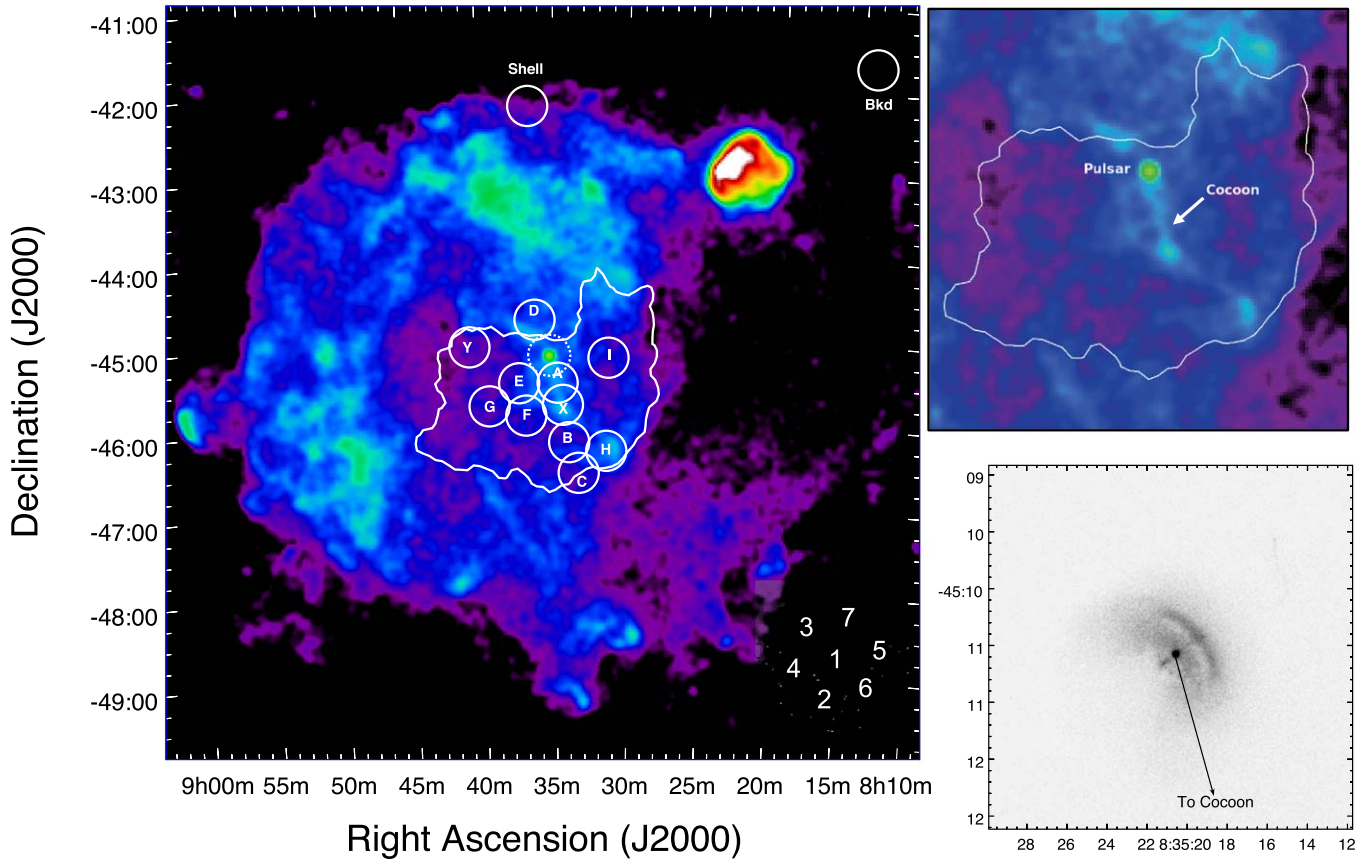

Figure 1. Left: *ROSAT* image of the Vela SNR (G263.9−3.3). Soft emission is shown in red and hard emission is shown in blue/green. The contour is the outer radio boundary of Vela X. The individual circles identify *XMM* pointings discussed in the text. The dashed circular region was taken in small-window mode and was used for imaging, but not for spectral analysis. The numbered circles in the lower right illustrate regions used for spectral fitting of each pointing (see Figure 6). Upper right: zoomed-in region of *ROSAT* image showing pulsar and cocoon. The outermost radio contour is shown to illustrate the extent of Vela X. Lower right: *Chandra* image of the Vela pulsar and its surrounding compact nebula. The jet axis is in the SE–NW direction, roughly aligned with the pulsar proper motion. The direction to the Vela X cocoon is indicated.

observations show that the pulsar is surrounded by a compact nebula (Figure 1, lower right) with distinct features corresponding to an inclined jet-torus structure (Helfand et al. 2001). VLBI parallax measurements (Dodson et al. 2003) establish a distance $d = 287^{+19}_{-17}$ pc and a proper motion that, when combined with the torus inclination, establishes a pulsar velocity of $\sim$80 km s^{-1}. The proper motion is along the direction of the pulsar jet axis, providing evidence for alignment of the kick velocity with the pulsar spin axis.

Radio observations of Vela X reveal a morphology concentrated to the south of the pulsar itself, suggesting that the SNR RS has propagated more rapidly from the northern direction due to a higher ambient density, thus leading to disruption of the northern part of the PWN. Higher-resolution radio images (Bock et al. 1998) show a network of filamentary structure in the PWN, possibly formed by Rayleigh–Taylor (R-T) instabilities in this interaction with the RS (Figure 2). *ROSAT* observations of the Vela X region (Markwardt & Ögelman 1995) reveal a large emission structure—the so-called "cocoon"—extending $\sim$45 arcmin to the south of the pulsar (seen as a distinct blue structure in Figure 1, upper right). The region is characterized by a hard spectrum and appears to lie along a bright elongated radio structure (Frail et al. 1997). ASCA observations established a two-component X-ray spectrum, with the hard component adequately described by either a power law or a hot thermal plasma (Markwardt & Ögelman 1997). Radio polarization maps show that the magnetic field in Vela X is roughly aligned with the cocoon in the central region (Bock et al. 2002).

Using the *CANGAROO* telescope, Yoshikoshi et al. (1997) detected γ-ray emission at energies above 2.5 TeV, located somewhat southeast of the pulsar. Assuming inverse-Compton scattering off of the same electron population responsible for the hard X-ray spectrum, they estimated a magnetic field strength $B \lesssim 4\,\mu$G. Subsequent observations with *H.E.S.S.* identified a TeV nebula larger than the X-ray cocoon, with a spectrum consistent with either a broken power law or a single power law with an exponential cutoff (Aharonian et al. 2006). The brightest region of TeV emission is concentrated along the X-ray cocoon. Using *XMM* observations along the central region of the cocoon, LaMassa et al. (2008) detected two distinct emission components—a power law with a spectral index of $\sim$2.2 and a thermal plasma with enhanced abundances of O, Ne, and Mg, presumably associated with ejecta that have been mixed into the PWN upon interaction with the RS. Broadband spectral modeling showed that the radio, non-thermal X-ray, and TeV γ-ray emission can be understood as the result of synchrotron and IC emission, but with a broken power law or a distinct population of radio-emitting electrons. A magnetic field strength of $\sim$5 μG was estimated, consistent with the value estimated from TeV studies. Modeling by de Jager et al. (2008) predicted observable GeV emission from Vela X based on a leptonic model for the TeV emission. The

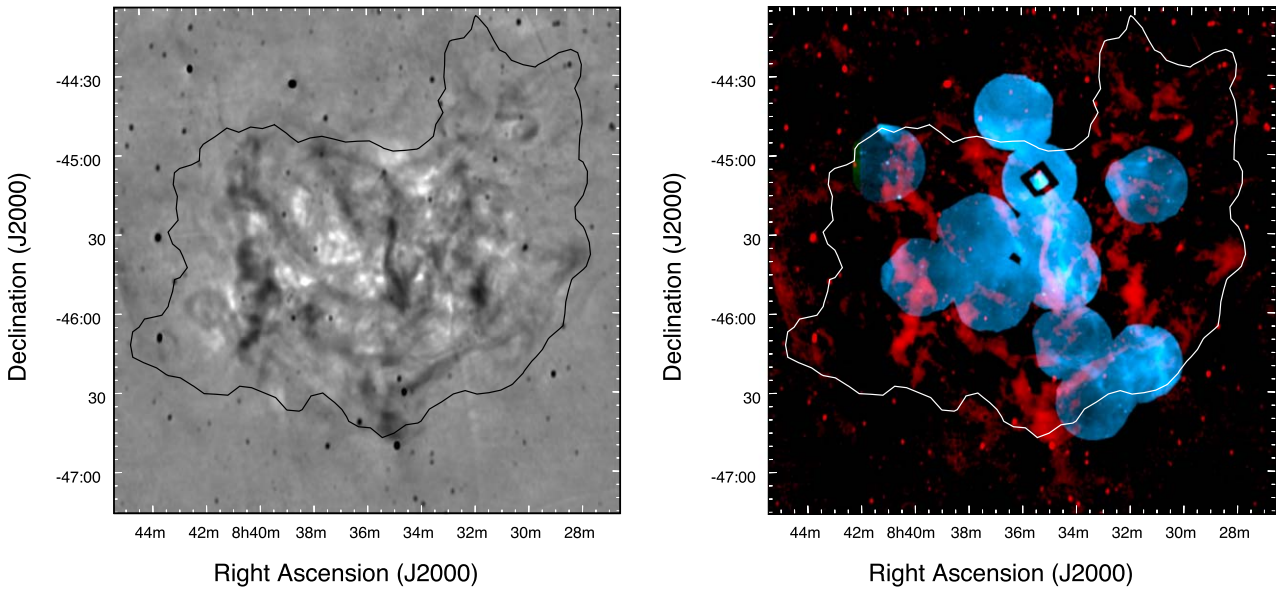

Figure 2. Left: *MOST* radio image of Vela X showing filamentary structure within the extended nebula. The single contour is the outermost contour from the diffuse radio emission in Vela X. The white regions in the image correspond to negative fluxes associated with missing coverage due to a lack of small baselines. Right: exposure-corrected mosaic of *XMM* pointing in Vela X, shown in blue, along with the *MOST* radio image, shown in red. The bright, elongated radio structure in the central region lies adjacent to the X-ray cocoon.

PWN is observed at energies up to ∼200 keV with *BeppoSAX* (Mangano et al. 2005), and observations with *Fermi* reveal γ-ray emission extended over the entire radio-emitting region, but with a centroid that is distinctly offset toward the west from the peak of the TeV emission (Abdo et al. 2010). X-ray observations with *Suzaku* (Katsuda et al. 2011) identify nonthermal emission in the northeast that appears to extend beyond the radio emission, leading to the suggestion that perhaps the X-ray and radio-emitting components are associated with different electron populations.

Here, we describe X-ray observations carried out in an *XMM* Large Project to study Vela X, along with *Chandra* observations coincident with the early region studied by LaMassa et al. (2008). We apply a hydrodynamical model, constrained by the observed properties of Vela X, to investigate the formation of the cocoon structure. In Section 2, we describe our observations and data reduction. The results of our spectral analysis are presented in Section 3, and our hydrodynamical simulations of the Vela SNR and Vela X are described in Section 4. We present a discussion of our results in the context of the multiwavelength data on Vela X in Section 5, and summarize our conclusions in Section 6.

2. Observations and Data Reduction

2.1. XMM

Vela X was observed for a total of 371 ks in eight pointings as an *XMM* Large Project carried out between 2009 April 30 and December 21. The individual pointings are identified as regions A–H in Figure 1, and the exposure times are summarized in Table 1. An additional 55 ks observation (region I) was obtained on 2011 May 22 at a position corresponding to the peak of the GeV emission measured with the *Fermi*-LAT (Abdo et al. 2010). The observations were carried out in full frame mode.

Additional archival observations from the interior of Vela X (regions X and Y) were also included in the analysis. A pointing at the pulsar, taken in Large Window mode (the dotted circle in Figure 1) was included in images of the system, but was not used in the spectral analysis. A pointing along the northern shell of the Vela SNR ("Shell" region) was used to constrain the column density and thermal contributions from the SNR rim. The SNR spectrum was extracted from a circular region with a 4.3 arcmin radius at the center of the detector, while a pointing outside the SNR was used to obtain a background spectrum ("Bkd" pointing). All data were reprocessed and cleaned with *SAS Version 15.0.0*. The cleaned exposure times for each EPIC detector are shown in Table 1.

An exposure-corrected image from the *XMM* observations is shown in Figure 2 (right), overlaid on the radio image. The

Table 1
Vela X Observations

ObsID	Pointing	Exp. (ks)	Clean Exp. (M1/M2/pn)	Date
		XMM-Newton		
0603510101	A	25	15.6/15.8/8.3	2009 Jun 30
0603510201	B	67	51.5/52.5/37.7	2009 Apr 30
0603510301	C	90	87.3/89.9/62.7	2009 Dec 21
0603510401	D	20	22.6/22.8/18.5	2009 Oct 17
0603510501	E	38	39.6/39.7/32.8	2009 May 20
0603510601	F	41	43.3/43.7/31.5	2009 May 10
0603510701	G	68	55.5/63.9/34.0	2009 Jun 09
0603510901	H	41	42.2/4.3.3/28.9	2009 Jun 15
0672040101	I	55	53.1/53.9/31.2	2011 May 20
0094630101	X	21	20.6/20.4/16.2	2002 May 02
0506490101	Y	45	34.0/30.4/21.3	2007 May 29
0153350101	bkdg	13.9	12.6/12.0/9.5	2002 Oct 14
0203960101	shell	27	26.6/26.9/15.1	2004 Oct 30
		Chandra		
12697	X	25	23.1	2010 Sep 28

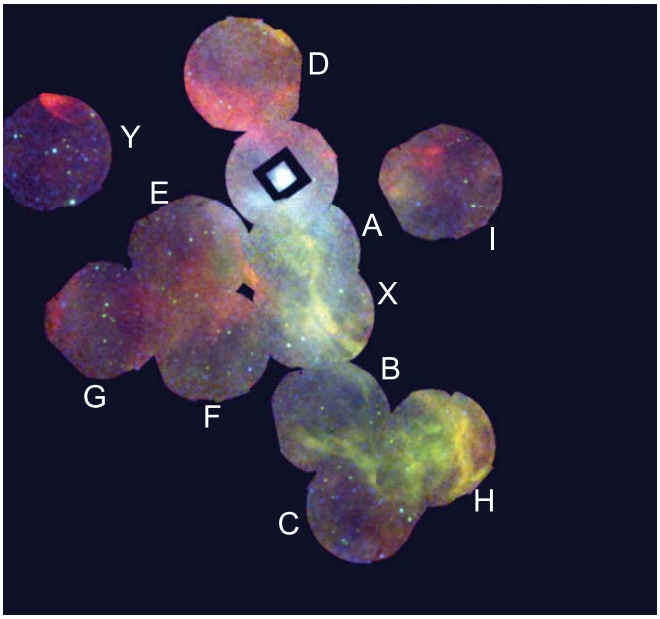

Figure 3. Exposure-corrected mosaic of Vela X regions covered by *XMM*, with red/green/blue representing energy ranges 0.4–0.75/0.75–1.4/2.0–7.2 keV. The cocoon structure is evident as a region of harder emission extending to the south/southwest from the pulsar, located within the small window in an upper pointing. (Note that the pointing containing the pulsar was not used in subsequent spectral analysis because of incomplete coverage due to the small-window mode.)

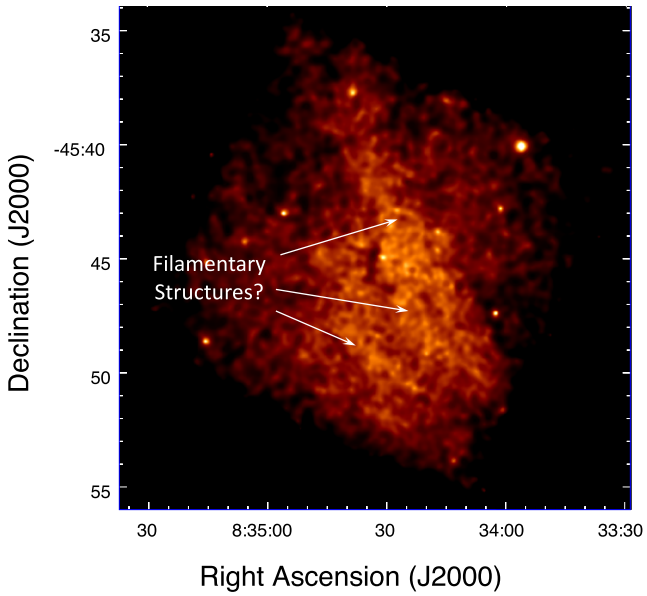

Figure 4. Exposure-corrected, adaptively smoothed ACIS image of the central portion of the Vela X cocoon (largely overlapping Region X in Figure 1). The structure is primarily composed of confined diffuse emission, although there is some evidence of narrow filamentary structures within the cocoon.

extended X-ray cocoon resides along, but distinct from, an extended radio structure. A three-color image from the *XMM* mosaic is shown in Figure 3. The cocoon structure is evident as a long feature that extends toward the southern regions of the PWN. Distinct filamentary structures are also observed in the south, and there are noticeable spatial variations in the soft emission identified in red. We discuss the spectra from these regions in Section 3.

2.2. *Chandra*

A portion of Vela X was observed with *Chandra* on 2010 September 28. The observation (ObsID 12697) was carried out with ACIS-I in Very Faint mode, with the pointing centered on the position of *XMM* field X (see Figure 1). Data were reprocessed and cleaned with *Ciao Version 4.8* resulting in a total exposure of 23.1 ks.

In order to investigate the spatial structure from this region of the Vela X cocoon, we created an adaptively smoothed, exposure-corrected image using a Gaussian smoothing kernel with a minimum of 100 counts on a logarithmic size scale ranging from 0.1 to 50 pixels (using a bin size of 4 ACIS pixels, or approximately $2'' \times 2''$). The image is shown in Figure 4. The overall extended morphology is similar to that observed with *XMM*, although there is some evidence for filamentary structure in the X-ray emission.

3. Spectral Analysis

To investigate the X-ray emission from Vela X, we concentrated on searches for nonthermal emission from the PWN, along with thermal emission from any ejecta component that may have been mixed into the nebula by the RS interaction. (Projected emission from the SNR shell was modeled as well, as discussed below.) Spectral modeling was carried out using XSPEC 12.9.0D with ATOMDB 3.03. For each of the eleven *XMM* pointings described in Table 1 (excluding the background and shell pointings), we defined seven circular regions (in detector coordinates), with radii of 4.3 arcmin, that approximately covered the detector field. Due to the large size of Vela X, and of the Vela SNR, local background subtraction is not possible. We thus followed the treatment for extended source analysis described in the *XMM* ESAS document.[9] For each region in each pointing, we eliminated point sources and then subtracted an internal background contribution for each detector using filter wheel closed data. We then defined a sky background model that consists of contributions from the diffuse extragalactic background (a power law with $\Gamma = 1.46$ and surface brightness 10.5 photons $\mathrm{cm}^{-2}\,\mathrm{s}^{-1}\,\mathrm{keV}^{-1}\,\mathrm{sr}^{-1}$ at 1 keV); a nonequilibrium ionization (NEI) plasma model (VNEI in XSPEC) for the projected contribution from the Vela SNR shell; an equilibrium plasma model (APEC) for the integrated contributions from hot gas in the Galactic plane; and an unabsorbed equilibrium plasma model for emission from the Local Bubble. Absorption was modeled with the TBABS model, and abundances were set to those from (Wilms et al. 2000). Residual internal background was modeled with a power law with additional Gaussian lines and 1.48 keV and (for MOS only) 1.75 keV corresponding to fluorescence from Al and Si; these components were not folded through the effective area (arf) file. For each region, the free parameters for the non-internal background components were fixed to be the same for each detector (but allowed to vary from region to region). The contributions from Vela X were modeled by an absorbed power law and an NEI plasma with variable abundances, corresponding to emission from the PWN and from ejecta. The absorption for the Vela shell, PWN, and ejecta components were tied together, as was the absorption for the Galactic

[9] https://heasarc.gsfc.nasa.gov/docs/xmm/xmmhp_xmmesas.html; see also (Snowden et al. 2008) and (Kuntz & Snowden 2008).

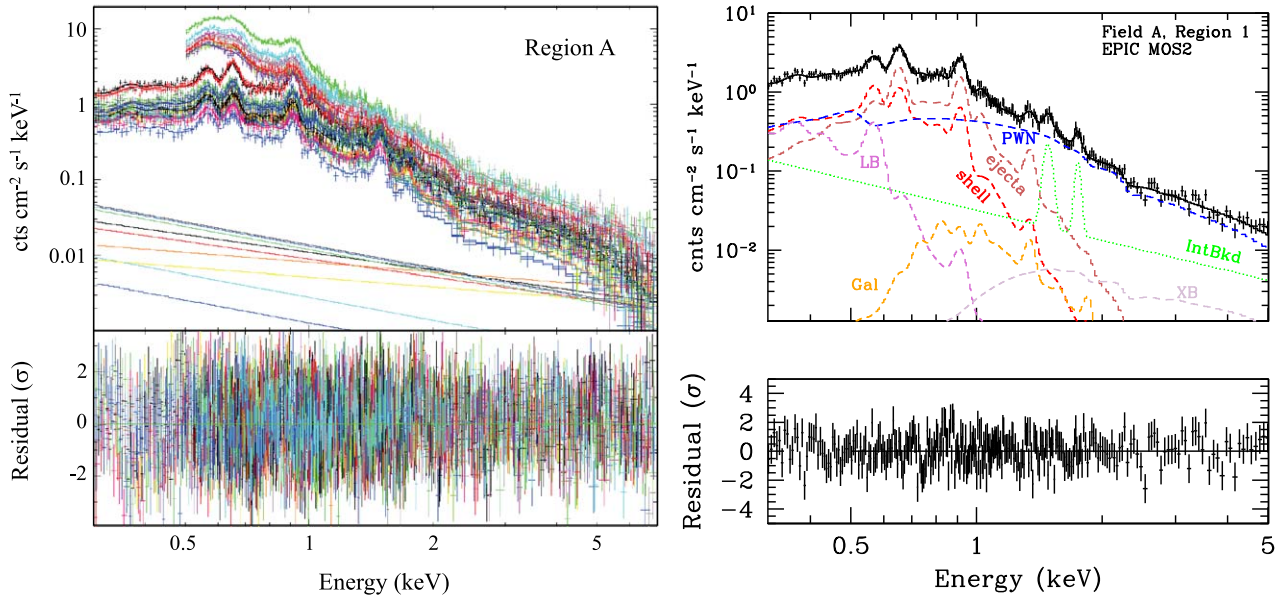

Figure 5. Left: joint fit to all MOS and pn spectra from Region A. The reduced chi-squared for the joint fit is $\chi_r^2 = 1.2$. The lines in the lower portion of the plot correspond to the power-law component of the internal background model. Right: MOS2 spectrum of the center region from Field A showing the model components described in the text.

thermal emission and extragalactic X-ray background components.

To establish the properties for the SNR shell, we first modeled the spectrum from the Shell region identified in Figure 1, using the above model without the Vela X contributions. We simultaneously fit the spectrum from the Bkd region, using only the background components described above. We found that the remnant shell is adequately described ($\chi_r^2 = 1.2$) by an NEI model with $kT_{\rm SNR} = 0.22$ keV with a neon abundance [Ne] = 2.8 relative to ISM values, an ionization timescale $\tau = n_e t \sim 10^{13}$ cm^{-3} s (i.e., effectively in equilibrium, possibly suggesting a high density component that could be associated with clumps, although τ is not well-determined around equilibrium, and could be as low as $\sim 2 \times 10^{12}$ cm^{-3}) and an absorption column $N_{\rm H} = 10^{20}$ cm^{-2}, in good agreement with results from Miceli et al. (2005). We fixed these values in our fits for the Vela X regions, along with the temperature of the Local Bubble contribution ($kT = 0.1$ keV). The normalization of the projected SNR emission within Vela X was allowed to vary from region to region to account for potential variations in the surface brightness.

For each *XMM* pointing on Vela X, we followed the same procedure, treating each region independently, and simultaneously fitting the background. The parameters for the sky background components and for the column density for the Vela SNR were fixed at values determined from the fit for the Shell region, except for the normalizations (other than that for the diffuse extragalactic component). In addition to the associated normalizations, the power-law index for the PWN component and the temperature and ionization timescale for the ejecta component, along with its abundances of O and Ne, were treated as free parameters.

The left panel of Figure 5 shows the joint fit for all regions in Vela X Pointing A. While the overall fit is reasonably good ($\chi_r^2 = 1.2$), it is important to note that by fitting all spectra from these regions simultaneously, we are potentially hiding some variations in the individual spectra. Our purpose here is to establish the presence of emission from the PWN and ejecta, and to search for global variations in the power-law index, temperature, and abundances. As discussed further below, the temperature of the ejecta component is only a small amount higher than that of the SNR shell, leading to a degeneracy between these components in regions where the temperatures are very close, or where the ejecta component is faint. The quality of the joint fits for the different regions range between $\chi_r^2 \approx 1.2$–1.3 along the cocoon, and $\chi_r^2 \approx 1.3$–1.5 in the outer regions.

Figure 5 (right) illustrates the different model components for the MOS2 spectrum from the central portion (Region 1) of pointing A. The Galactic thermal (Gal) and extragalactic (XB) background components contribute little to the overall emission, and the emission from the Local Bubble contributes only at the lowest energies, at and below the O VII line at 0.56 keV. The power-law component from the residual internal background is only significant at high energies, but the two fluorescence lines are readily seen in the full spectrum. For this region, nonthermal emission from the PWN dominates above 1 keV, and the thermal emission from the ejecta component shows significantly enhanced Ne, O, and Mg abundances. The model fit yields $\chi_r^2 = 1.0$.

Nonthermal emission is detected throughout Vela X, with the observed spectral index varying spatially over a range $\Gamma \sim 1.9$–3.2, with the exception of Region Y, which shows anomalously low values in some regions (possibly related to a considerably higher hard internal background component than observed in the other fields, which may be compromising our ability to constrain any PWN emission). A spectral index map is shown in Figure 6 (left). The spectrum is hardest near the pulsar, with a distinct steepening at larger distances; regions adjacent to the pulsar show $\Gamma \sim 2$, while those at the outer edges of the PWN show values of $\Gamma \sim 3$. The spectrum is harder along the cocoon region (and along the extended direction to the south) than in other regions of Vela X. Interestingly, the spectrum in Region I, corresponding to the peak of the *Fermi*-LAT emission, appears harder than regions

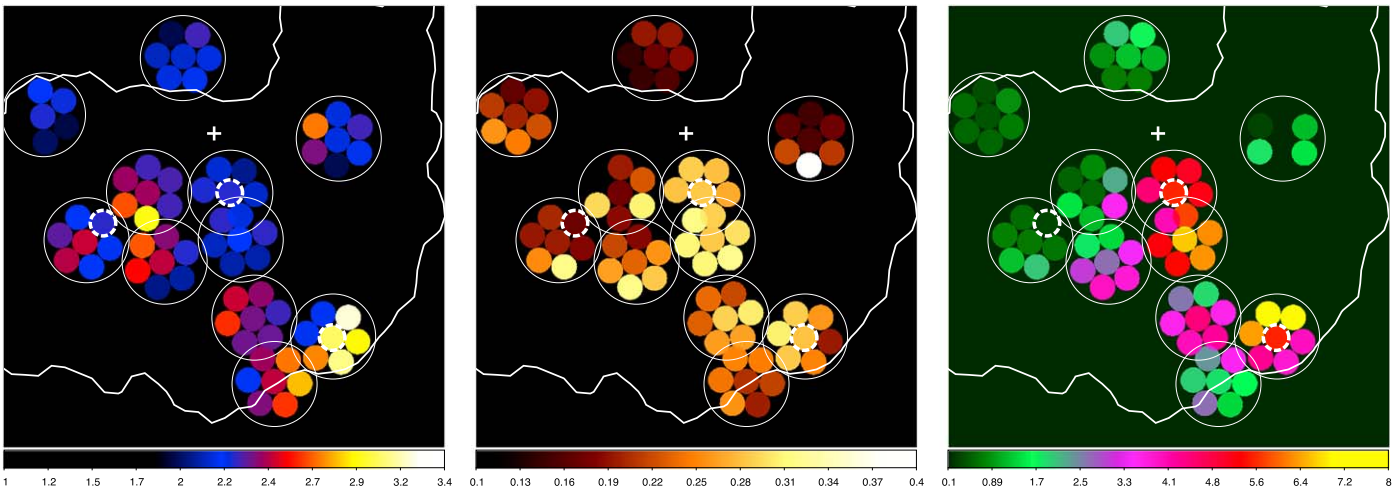

Figure 6. Maps of the power-law index (left), temperature in keV (middle), and Ne abundance relative to the ISM value (right) from spectral fits of subregions in *XMM* pointings in Vela X. The temperature and abundance correspond to the ejecta component in the spectral model. The outermost radio contours provide the rough outline of the PWN and the cross indicates the position of the pulsar. The color bars indicate the values for the photon index, the temperature in keV, and the abundance relative to solar values, respectively. The parameter uncertainties vary from region to region, but are typically $\lesssim$0.05–0.1 for the spectral index, $\sim$0.01 keV for the temperature, and $\sim$0.1–0.3 for the abundance. Distinct spectral steepening is observed along the cocoon, which also shows higher temperatures and abundances than other regions within the PWN. For reference, region 7 for each of the pointings (see inset to Figure 1, left) is identified with a red dot in the center panel. The dashed circles correspond to regions for which spectra are shown in Figure 7.

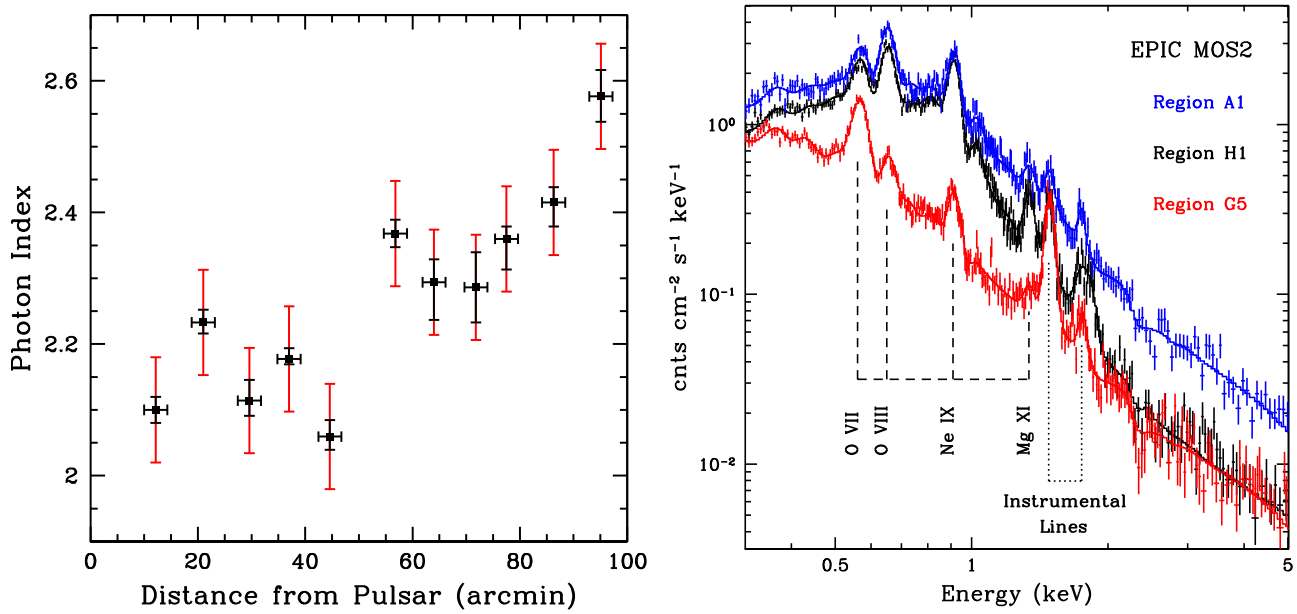

Figure 7. Left: variation in spectral index with distance from pulsar along Vela X cocoon. A distinct spectral steepening is observed at large distances along the cocoon. Black error bars correspond to 90% confidence uncertainties from the joint fits while the red error bars represent systematic errors estimated by comparing values from the fits with those obtained by fitting individual regions from a given pointing separately. Right: spectra from regions A1, H1, and G5 which show increasingly lower temperatures. The reduced amount of O VIII (relative to O VII) and Mg X1 emission in Region G5 provides particular evidence for the lower temperature. (See also Figure 8.)

at similar distances on the other side of the cocoon. The spectral index from regions along the direction of the cocoon, and extending to the edge of the PWN in the south, along the cocoon, is shown in Figure 7 (left). A significant steepening is evident at larger distances, indicating that synchrotron losses are significant for regions far from the pulsar. Uncertainties in the index vary from region to region, but are typically $\lesssim$0.05–0.1 (90% CL).

We detect a significant thermal component within Vela X that appears to be associated with hot ejecta, with enhanced abundances of Ne and O in regions along the cocoon (as well as enhanced Mg in some fits of individual regions). The temperature varies throughout the PWN ($kT \sim 0.14$–0.32) but is hottest along the filamentary regions seen in Figure 3. A map of the temperature distribution is shown in Figure 6 (center). The ionization timescale of this thermal component is high throughout the PWN, consistent with the plasma being in ionization equilibrium. The O and Ne abundances are highest near the cocoon, suggesting that the ejecta component is dynamically concentrated in this structure; pointings A, X, B, and H have O (Ne) abundances that are 3–8 (2–5) times higher than ISM values (Figure 6, right). For other regions, both the

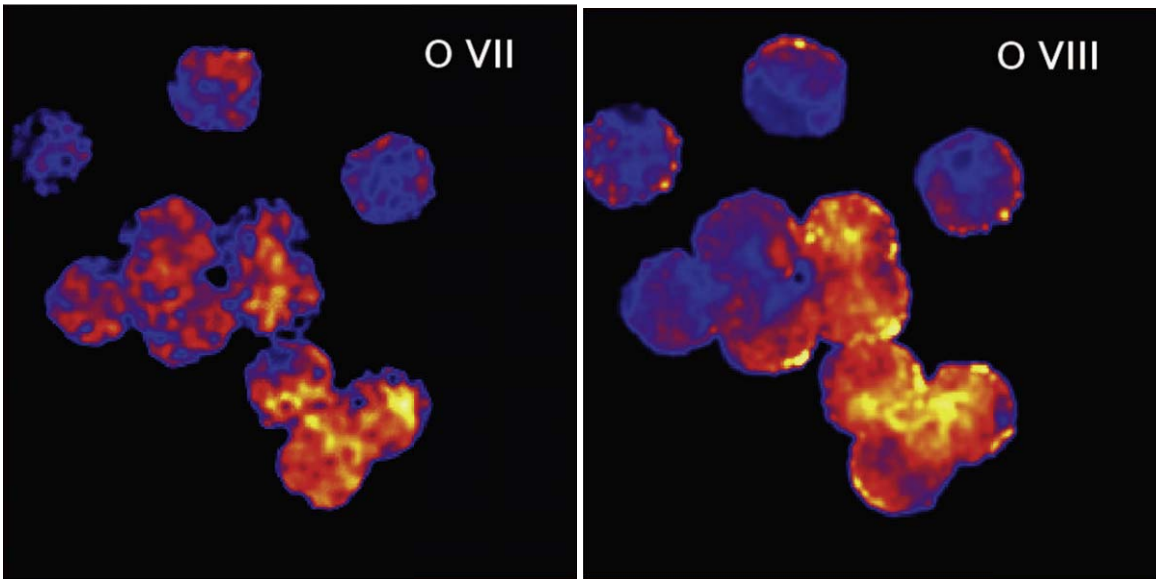

Figure 8. Equivalent-width maps (see the text for a definition) for O VII and O VIII lines in Vela X. Note the close correlation between the O VIII map and the temperature map in Figure 6 (center). Edge-brightening along the outskirts of some regions is an artifact associated with the rapidly declining effective area at the edge of the detector.

temperature and the abundances are more similar to those for the SNR shell emission component, indicating that any ejecta emission is dominated by the projected emission from the shell.

Given that the SNR shell shows both variations in brightness and enhanced abundances of Ne, it is not impossible that the emission we are associating with an ejecta component actually corresponds to anomalous thermal regions from the shell, seen in projection. However, the good correspondence between this thermal component and the nonthermal emission, which is not seen anywhere else along the SNR shell, makes this extremely unlikely. The enhanced abundance of Mg seen in individual fits to Region 1 in Pointing A support this picture as well.

The variations in both PWN emission components are illustrated in Figure 7 (left), where we compare MOS2 spectra from three distinct regions within Vela X (indicated by dashed circles in Figure 6). It is clear, for example, that the nonthermal contribution in region H1 is much lower than that in A1, despite the thermal flux being similar, albeit with a lower temperature in H1. Region G5 shows a significantly lower temperature. Also evident is a significant variation in the strength of the emission lines. Variations in the ratio of O VIII to O VII are easily observed.

The relative strengths of the O VII and O VIII lines within Vela X are illustrated in the line-to-continuum maps shown in Figure 8. The maps were created by extracting images in the energy ranges 480–615 keV and 615–715 keV for the two respective lines, and estimating the continuum in each line region through an interpolation of the continuum regions in the range 425–475 keV and 1120–1160 keV range, assuming a power-law behavior for the continuum over this range. The regions with enhanced O VIII emission relative to that from O VII are seen to correlate with the temperature map in Figure 6 (center). This is expected, with the lower temperature plasma producing weaker emission from the higher ionization state, but is also consistent with the cooler SNR component dominating the ejecta emission in these regions.

4. Modeling

Both the morphology of the Vela SNR and estimates of the density in regions around the remnant suggest that the surrounding density is higher in the NE than in the southwest (SW). This is consistent with the notion that the structure of Vela X, with the bulk of the PWN located to the south of the pulsar, is the result of the SNR RS propagating more rapidly from the NE (Blondin et al. 2001). To better understand the structure of Vela X, it is necessary to consider models for the evolution of the entire composite system.

4.1. Analytical Modeling

We note that multiple studies indicate that the medium surrounding the Vela SNR contains clumps or small clouds (e.g., Nichols & Slavin 2004; Miceli et al. 2005), complicating our treatment of the density profile. A similarity solution for the evolution of an SNR in a cloudy medium was developed by White & Long (1991, WL91 hereafter) by introducing two additional variables to the Sedov solution—the mass ratio of cloud material to intercloud material in the SNR (C), and the ratio of the cloud evaporation timescale to the age of the SNR. The evolution of the SNR radius is similar to that found from a Sedov solution, but for a density that is weighted toward larger values than that of the intercloud medium, due to contributions from additional material evaporated from the engulfed clouds. While MHD simulations that incorporate realistic cloud size distributions and a full treatment of the thermal conduction effects show considerable deviations from the WL91 solutions (Slavin et al. 2017), the associated behavior of the expansion law is still a reasonable approximation. This is illustrated in Figure 9, in which we plot the radius as a function of time for three simulations by Slavin et al. (2017) using different filling factors of clouds with a factor of 100 density contrast with the intercloud medium (shown as solid curves). For each, we plot (as dashed curves) Sedov solutions using fixed density values shown in the figure. While a full treatment of a composite SNR

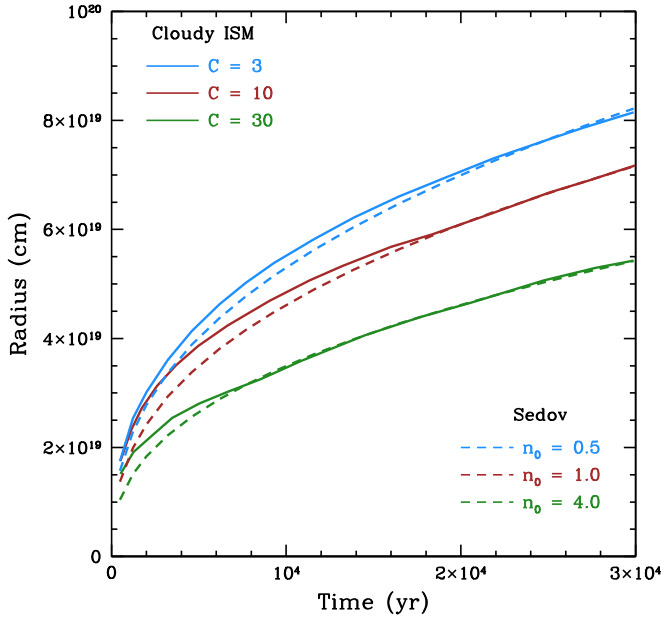

Figure 9. SNR radius evolution for expansion in a cloudy ISM (solid), and the Sedov solution (dashed) for evolution into a uniform medium, both for $E_{51} = 1$. The cloudy ISM curves (from Slavin et al. 2017) assume density values of 0.25 (25) cm^{-3} for the intercloud (cloud) regions. The value of C corresponds to the ratio of the cloud mass to that of the intercloud medium. The Sedov solution curves provide reasonable approximations assuming densities roughly connected to the evaporated cloud density in the cloudy ISM model.

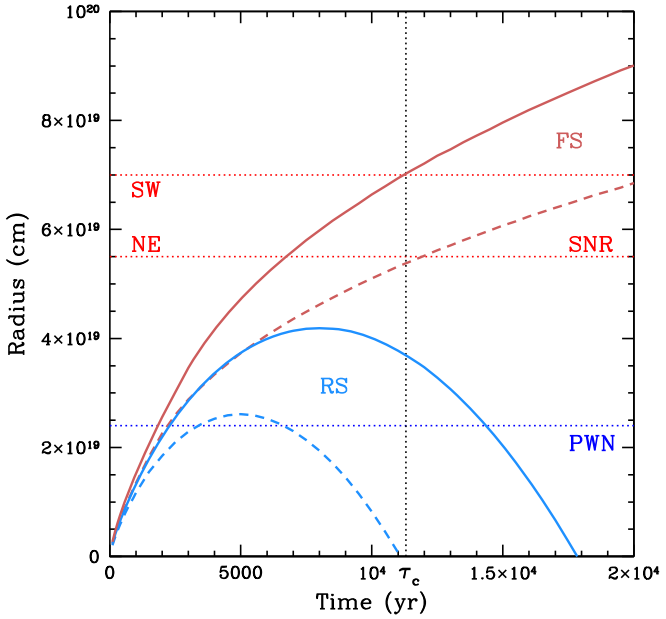

Figure 10. Forward (red) and reverse (blue) shock evolution with time, using the solutions of Truelove & McKee (1999). The solid (dashed) curves correspond to ambient densities of $n_0 = 0.15$ (0.5) cm^{-3} with $E_{51} = 1$, $M_{\mathrm{ej}} = 8M_{\odot}$, and a power-law index $n = 12$ for the outer ejecta.

evolving into a cloudy ISM is beyond the scope of this paper, Figure 9 illustrates that evolution at a fixed density (larger than that of the intercloud material, but much smaller than that for the clouds) provides an adequate description.

Sushch et al. (2011) have simulated the evolution of the Vela SNR using exactly this approach with the WL91 solutions. They assume a higher concentration of clouds in the NE region of the SNR, leading to a larger effective density in this direction than in the SW, which they suggest may be due to the presence of a stellar wind bubble blown by a nearby Wolf–Rayet star, in the γ^2 Velorum binary system, creating a step-like density increase from the SW to the NE. Models of the radio emission predicted from such a scenario are able to reproduce the major observed radio properties of the Vela SNR (Sushch & Hnatyk 2014). Here, we make a similar assumption about an overall density profile that increases from the SW to the NE.

An important constraint on the properties of this surrounding medium is set by the morphology of Vela X, where the RS appears to have overtaken the pulsar from the NE direction. To investigate the basic evolutionary parameters of the SNR, we have used solutions of Truelove & McKee (1999) for the radius of the FS and the RS during evolution from the ejecta-dominated phase to the Sedov phase. While this ignores the effects of the PWN, it provides a framework in which to investigate the basic evolution for different values of the ambient density, explosion energy, ejecta mass, and ejecta density profile.

In Figure 10 we plot solutions for the FS (red) and RS (blue) radius for two different ambient densities. We have chosen values that yield the observed FS radius in the NE and SW at $t = \tau_c$, the characteristic age of the pulsar. We have assumed an ejecta profile with a constant-density core that transitions to a steep power law at larger radii Chevalier (1982). We have used a power-law index $n = 12$, which is typical of core-collapse supernovae (e.g., Chevalier 1982; Matzner & McKee 1999), although the profile is quite similar for $n = 9$. We have adjusted the ejecta mass until we obtained solutions that provide an RS radius that has evolved completely back to the SNR center from the NE direction. The RS from the SW direction would, in this case, not yet have reached the southern portions of the PWN (whose extent is indicated by the dotted blue line), a result that does not hold with more detailed modeling (see below).

We note that, for different values of the braking index and the initial spin-down power, the actual age of the Vela Pulsar (and its SNR) may be considerably larger than τ_c. With no definitive value for the system age, here and below we use τ_c as a convenient age estimate to investigate the structure of Vela X. Similar results can be obtained using different values for these input parameters, accompanied by modifications of the ambient density.

4.2. Hydrodynamical Modeling

In an effort to understand the overall structure of Vela X in the context of the basic evolutionary picture described above, with particular interest in the cocoon region of the PWN, we have carried out modeling of the system using simulations with the VH-1 hydrodynamics code as modified to treat the evolution of an SNR expanding into an inhomogeneous medium, and with a central pulsar creating a PWN that expands into the interior ejecta. The model is based on that from Blondin et al. (2001), but also includes treatments for following the age of the particles injected by a moving pulsar and for tracking the mixing of ejecta into both the swept-up CSM and the PWN material (Kolb et al. 2017).

We modeled the pulsar wind as a high Lorentz factor wind from the pulsar, which we subsequently refer to as a relativistic component, though it is treated here as a $\gamma = 4/3$ fluid injected at the pulsar position (initially at the SNR center) with $\dot{M} = 2\dot{E}/v_w^2$. For computational purposes, the wind speed v_w was taken as $\sim 1.5 \times 10^9$ cm s^{-1}, considerably lower than the

actual electron injection speed for a PWN. This results in a high effective mass of electrons, but has no significant impact on the subsequent evolution (Kolb et al. 2017). The pulsar position was initially taken to be at the center of the SNR. In our initial 2D simulations, the pulsar was given a velocity of 61 km s^{-1} in a direction consistent with the observed proper motion.[10]

The pulsar spin-down power is evolved as

$$\dot{E}(t) = \dot{E}_0(t)\left(1 + \frac{t}{\tau_{\rm sd}}\right)^{-\frac{n+1}{n-1}}, \quad (1)$$

where $\tau_{\rm sd}$ is the spin-down timescale and n is the braking index. While measurements of the braking index for many middle-aged pulsars like the Vela pulsar are complicated by the presence of frequent glitches, Lyne et al. (1996) and Espinoza et al. (2017) have measured $n = 1.7 \pm 0.2$, well below the value $n = 3$ expected for standard magnetic dipole spin-down. Younger pulsars show braking indices closer to the dipole value, suggesting the possibility that extensive glitching behavior develops later, somehow connected with a change in the index. Increases in the superconducting component of the NS moment of inertia can lead to $n < 3$, as can a temporal increase in the surface magnetic field (as might occur through diffusion of a field initially buried under a non-magnetic crust formed from early fallback onto the NS; e.g., Page 2013). For our simulations, we have investigated both $n = 1.7$ and $n = 3$ and find that, in general, a smaller value for n can be compensated by an increase in the value of $\tau_{\rm sd}$, which would also result in a spin period at the current epoch that does not differ much from the period at birth.

We have treated the inferred density gradient into which the Vela SNR appears to be expanding by

$$\rho(z) = \rho_0\left[1 - \frac{2-x}{x}\tanh(z/H)\right]. \quad (2)$$

This represents a step-like transition between two constant-density regions, where z is the coordinate in the direction of the gradient, H is the size scale for the density transition, and x regulates the amplitude of the density step. We choose parameters that yield a density contrast of four across the SNR, as suggested by measurements described above. The input parameters for the HD model are summarized in Table 2.

Our initial simulations, in which the parameter space was explored, were carried out in 2D. In Figure 11 we show density profiles of the composite system at three discrete time steps in order to illustrate the overall evolution. The simulation uses a cylindrical 2D grid with 600 zones in both the r and ϕ directions. The circle in the center represents the position of the pulsar, and the surrounding light blue structure is the PWN. The external density increases from SW to NE as described by Equation (2). The dark inner region represents the unshocked wind, and the termination shock is at the boundary of these two regions. The FS is shown in red and the RS is orange. The ISM and ejecta regions are separated at the contact discontinuity where Rayleigh–Taylor instabilities are evident.

At an age of 2500 years, the asymmetric propagation of the RS is evident, with the shock approaching the PWN from the NE, but still far from the nebula in the SW. By 4000 years the RS has encountered the PWN in the NE, sweeping PWN gas back toward the location of the pulsar. By an age of 7500 years the entire PWN has been disrupted by the RS, with the component arriving from the NE completely sweeping over the pulsar, creating an apparent trail of emission to the south.

[10] In the simulation, the pulsar is kept stationary at the center of the grid, while the rest of the grid is given a velocity opposite that of the pulsar proper motion.

Table 2
HD Model Parameters

Parameter	Description	Value
Input Parameters		
v_p(km s^{-1})	Pulsar velocity	61
v_p direction (deg)		31
E_{51} (10^{51} erg)	Explosion energy	1
$M_{\rm ej}$ ($M_\odot$)	Ejecta Mass	5
$n_{\rm ej}$	Ejecta density profile index	12
$\dot{E}_0$(erg s^{-1})	Initial spin-down power	10^{39}
n	Braking index	3.0
τ_0 (yr)	Spin-down timescale	1000
$n_{0,\rm min}$(cm^{-3})	Minimum ambient density	0.18
x	n contrast parameter[a]	1.25
H (pc)	n contrast length scale	6.5
n_0 gradient (deg)	North of west	121
Simulation Output		
$R_{\rm SNR,NE}$ (cm)	SNR Radius (NE)	5.7×10^{19}
$R_{\rm SNR,SW}$ (cm)	SNR Radius (SW)	7.1×10^{19}
$l_{\rm cocoon}$ (cm)	Cocoon length	1.8×10^{19}
$\dot{E}$(erg s^{-1})	Current spin-down power	6.6×10^{36}

Note.
[a] Parameter required to produce density contrast of four from SW to NE.

In Figure 12 we show the system at an age of 11.3 kyr, matching the Vela Pulsar characteristic age, here in a 3D simulation using the parameters arrived out for our 2D modeling. The 3D simulation was computed on a spherical Yin-Yang grid (Wongwathanarat et al. 2010) using 384 radial zones and an angular resolution of 56.′25. The pulsar has been given a kick of 80.2 km s^{-1} such that the velocity component along the plane in Figure 12 is 61 km s^{-1} and the component along the line of sight is 52 km s^{-1} away from the observer. The projected direction of the pulsar motion, as well as the density gradient, are indicated with arrows. At this stage the RS has swept the pulsar wind far to the SW of the pulsar, creating a relic PWN infused with both relativistic gas and ejecta. The density scale (in g cm^{-3}) is shown in the legend, and the outer radio contour for Vela X (scaled in size assuming a distance of 290 pc) is shown for comparison. The red/orange regions are primarily ISM or ejecta, while the low-density blue regions have large concentrations of relativistic gas. The dashed box region is shown in an extended panel on the right. The black contour marks the boundary of the PWN, composed of both relativistic gas and mixed-in ejecta; material outside the contour is pure ejecta (or ISM in the outermost regions). Within the PWN region, turbulent vortex-like structures have created a stream of gas between the pulsar and the relic PWN whose properties appear very similar to the Vela X cocoon (discussed further below). The elongated structure is characterized by a dense filament of ejecta aligned with a similar structure of relativistic gas. The length scale of the structure is $\sim 1.5 \times 10^{19}$ cm, corresponding to an angular size of $\sim$57 arcmin at the distance of Vela X—slightly larger, but in

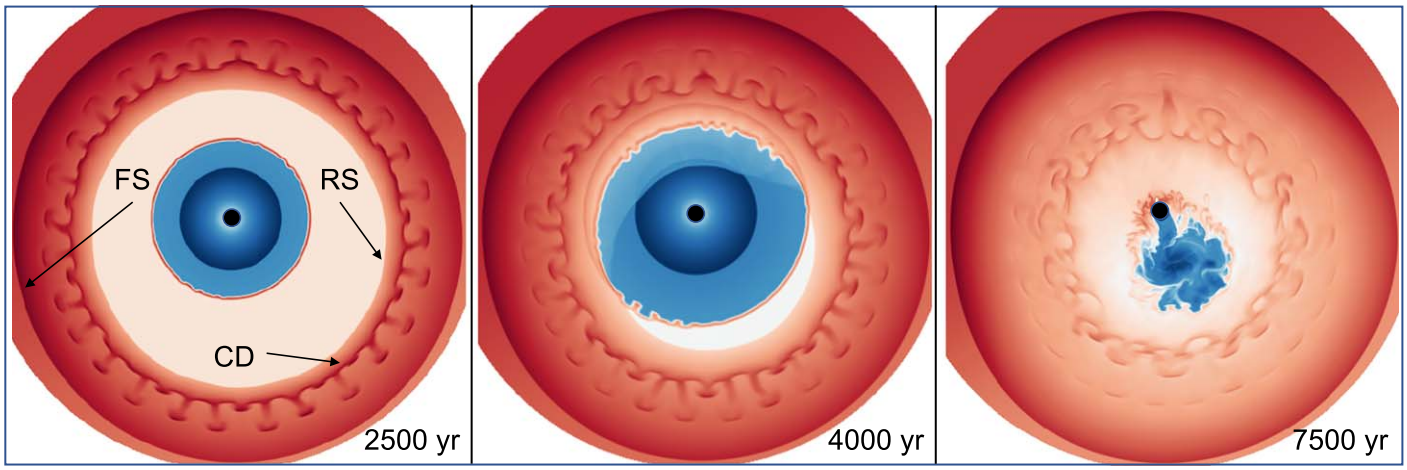

Figure 11. Hydrodynamical simulations of a composite SNR evolving into a density gradient. Each panel shows the density at a different stage of the evolution, with the lowest density regions (blue) corresponding to regions dominated by relativistic gas from the pulsar. The FS, RS, and contact discontinuity (CD) for the SNR are indicated in the left panel. The PWN becomes disrupted as the SNR RS propagates more rapidly from the NE, due to the external density gradient, eventually forming a relic nebula connected by a trail of emission from the pulsar. See the text for further discussion.

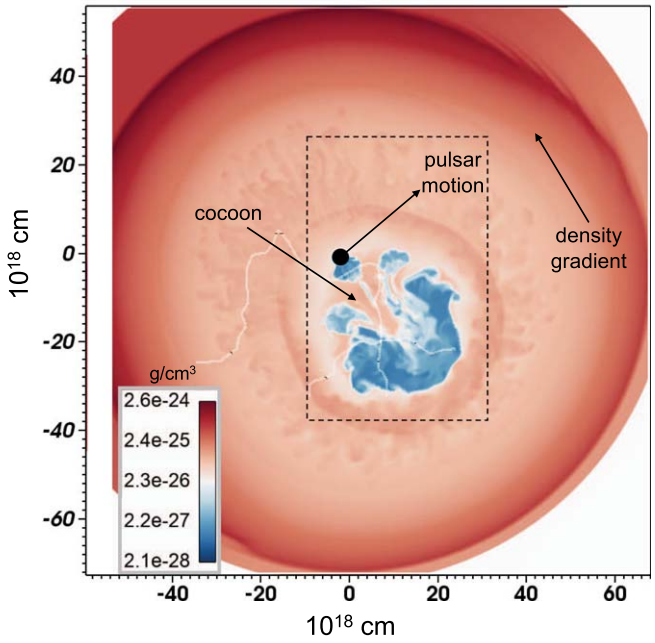

Figure 12. Simulation at the characteristic age of the Vela pulsar. The plot on the left represents the density, with the lowest density regions (blue) corresponding to regions dominated by relativistic gas from the pulsar. Note the channel of thermal gas beyond the wind immediately below the pulsar, extending into the relic PWN, corresponding to a structure similar to the Vela X cocoon. The black contour represents Vela X at a distance of 290 pc. The region within the dashed box is shown in Figure 13.

overall agreement with the ∼45 arcmin length of the Vela X cocoon.

5. Discussion

The gas distribution in the region of the disrupted PWN is a complex mix of relativistic particles from the pulsar and ejecta material swept up by the SNR RS. Figure 13(a) reproduces the total gas density in this region, with the legend indicating the scale in g cm^{-3}. As in Figure 12, low-density blue regions are dominated by relativistic material injected by the pulsar. Chaotic, elongated structures of ejecta and relativistic gas comprise the cocoon structure, while the relic PWN persists in the southernmost regions. Large amounts of ejecta are found throughout most of the structure, consistent with our detection of thermal gas with enhanced abundances in the spectra from Vela X. Regions along the cocoon have high density, presumably producing the bright elongated structures seen in Figure 3. These structures are similar to those first discussed by Chevalier & Reynolds (2011). Interestingly, while the innermost ejecta are expected to have a significant Fe component, the abundances derived from our spectral investigations are consistent with those expected to be found farther from the ejecta core. This may be indicative of significant mixing of the inner ejecta early in the evolution of the supernova that formed the system.

Figure 13(b) shows the density of just the relativistic gas in the hydro simulation, making it clear that one might expect synchrotron radiation from the entire PWN structure. The density along the cocoon-like structure is higher than that in the immediate surroundings, but not significantly higher than that in some other parts of the PWN.

While we are unable to calculate the magnetic field strength within the evolved PWN from our purely hydrodynamical simulations, it is instructive to investigate the age of the relativistic gas in different regions of the nebula in order to predict the general behavior of the associated synchrotron radiation. The characteristic synchrotron energy of an electron is given by

$$h\nu_s \approx 2.2 E_{e,100}^2 B_{10}\ \mathrm{keV}, \quad (3)$$

where $E_{e,100}$ is the electron energy in units of 100 TeV and B_{10} is the magnetic field strength in units of 10 μG, and the lifetime against synchrotron losses is

$$\tau_{\rm syn} \approx 820 E_{e,100}^{-1} B_{10}^{-2}\ \mathrm{years}. \quad (4)$$

For emission at 1 keV, and assuming a magnetic field strength of 5 μG based estimates for Vela X (LaMassa et al. 2008), the synchrotron lifetime of the electrons emitting X-rays in the soft band is ∼3.5 kyr (∼1.1 × 10^{11} s). The age (in seconds) of the relativistic gas in the PWN (i.e., the time since injection into the nebula) is shown in Figure 13(c). Particles in the saturated (dark blue) regions nearest the pulsar have ages less than $\tau_{\rm syn}$,

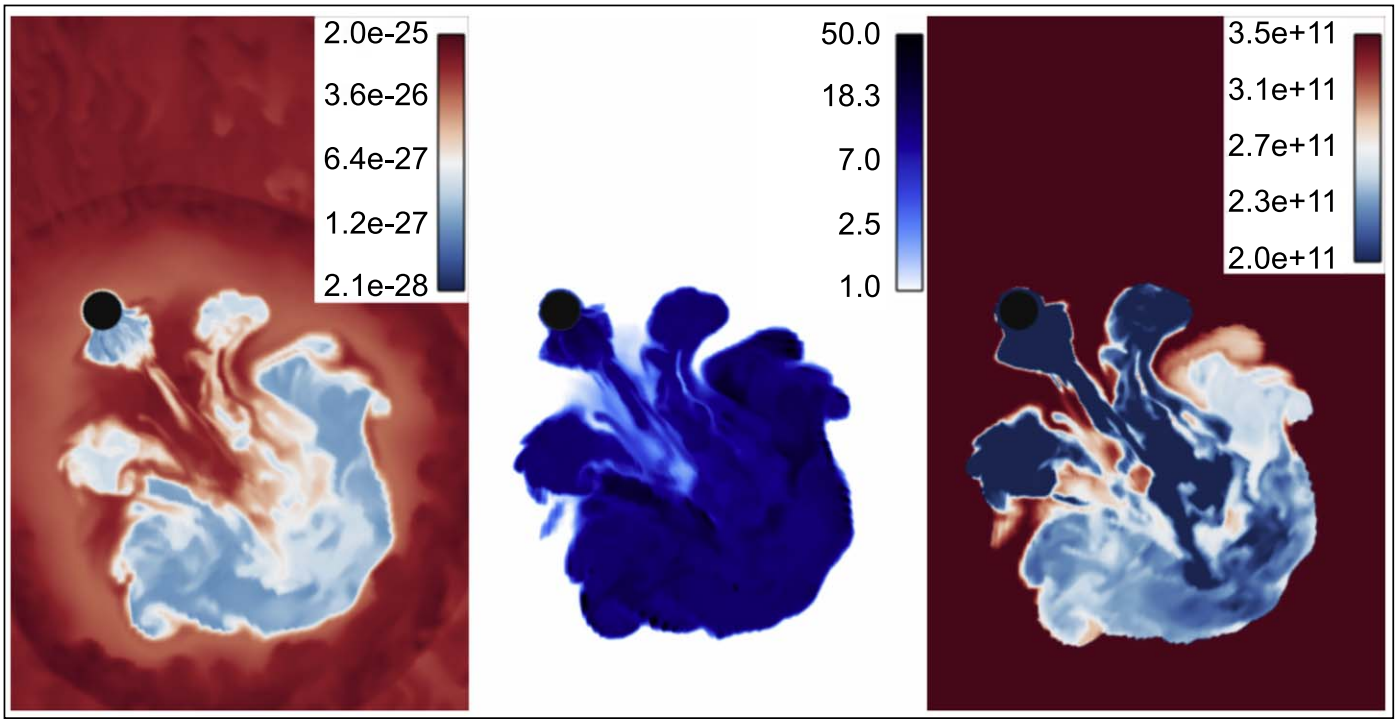

Figure 13. Inner regions of the Vela X HD simulation. Panel (a) shows the density (in g cm^{-3}). Here, the red/orange regions have higher density and are dominated by ejecta, while the blue regions are dominated by low-density PWN gas. Panel (b) shows the relative effective density of just the relativistic (PWN) gas. Panel (c) plots the age of the relativistic gas (in seconds since the gas entered the grid). Note that the scale is saturated at small timescales to emphasize the distribution of younger particles along the cocoon.

while those in the southern reaches of the cocoon and in the relic nebula have ages longer than the synchrotron loss time. This appears consistent with the observed variation in spectral index in Vela X, where the spectrum is hard in the inner regions but softer at large distance from the pulsar (see Figure 7).

The X-ray emission from pointing I, which overlaps the position at which the peak GeV emission is seen in *Fermi*-LAT observations, shows a harder nonthermal component than regions at similar distances on the opposite side of the cocoon. This is difficult to reconcile with the observed γ-ray properties of Vela X, which, along with the radio and X-ray data, seem to indicate two distinct electron populations, with the GeV emission being associated with the low-energy component (de Jager et al. 2008). Hinton et al. (2011) suggest that diffusion of particles from the relic nebula, which is proposed to contain an older population of particles, can explain both the observed steep GeV spectrum of Vela X and the observation that the GeV emission is more broadly distributed than the TeV emission. The harder X-ray spectrum at the GeV peak seems to contrast with this suggestion, although the considerable hydrodynamical transport of the PWN gas is observed to form pockets of younger gas within regions of older particles (Figure 13(c)). MHD simulations that can treat the particle diffusion along with the overall evolution of the magnetic field within the PWN are required to address this issue further. We note, also, that the jet from the Vela Pulsar shows a complex structure that extends toward the general direction of this region (e.g., Pavlov et al. 2003), although the scale of this structure appears quite small relative to the distance to this region.

Finally, we note that Vela X is considerably broader in directions perpendicular to the cocoon than the extent in our simulations, which we attribute to a more complex ambient density structure than the assumed smooth jump in a single direction. In addition, while the RS sweeps the entire relic PWN to the south of the pulsar in our simulations, we note that emission from Vela X is observed somewhat to the north of the Vela Pulsar. This may be a result of magnetic effects that are not properly modeled in the purely hydrodynamic simulations.

6. Conclusions

We have carried out X-ray observations and hydrodynamical simulations of Vela X in an effort to understand its overall structure in the context of the evolution of a PWN within the confines of an SNR. Our results show that the properties of Vela X are well described by a model in which the PWN has undergone asymmetric disruption from the SNR RS, resulting from the Vela SNR evolving in a non-uniform ISM with a higher density in the NE, as originally suggested by Blondin et al. (2001). Our large-scale mapping of key regions within Vela X provides important details on the overall structure that confirm earlier measurements of both thermal and nonthermal emission (Markwardt & Ögelman 1997; LaMassa et al. 2008). We produce temperature, abundance, spectral index, and equivalent-width maps that reveal significant variations in the properties of the thermal and nonthermal gas within Vela X. We find the following:

1. At an age equal to the characteristic age of the pulsar, the overall size of the SNR and PWN can be approximately reproduced assuming evolution into a density gradient whose values are constrained by previous density measurements for the Vela SNR.
2. The interior of Vela X contains both relativistic gas, producing synchrotron radiation, and ejecta material

whose thermal emission establishes enhanced abundances of Ne, O, and Mg. This is consistent with HD simulations that show significant mixing of ejecta into the PWN during the RS-crushing phase of evolution.

3. Equivalent-width maps show a complex variation in the relative contributions of O VII and O VIII to the emission. Both broad fitting of the ejecta temperature and modeling of spectra from discrete regions show that these variations are associated with temperature differences that are primarily associated with regions where the SNR shell component dominates emission from the ejecta.
4. The Vela X "cocoon" consists of an extended region whose emission is from a combination of ejecta and PWN material. High-resolution X-ray images provide some indication of fine-scale filamentation, but show that the structure is largely diffuse on small scales. Simulations show that such a structure can naturally be formed as part of the hydrodynamical development of the RS-PWN interaction.
5. The spectrum of the nonthermal emission is harder near the pulsar than at regions farther along the cocoon, and beyond. The HD simulations indicate that this is consistent with both the cocoon and the relic PWN being dominated by particles injected by the pulsar at an earlier age, now subject to synchrotron losses, while the region nearer the pulsar contains particles more recently injected by the pulsar.
6. The nonthermal X-ray spectrum at the peak position of the GeV emission observed with the *Fermi*-LAT appears harder than emission at similar offset distances from the pulsar and the cocoon.

The overall picture from our observations and simulations is consistent with the understanding that the overall morphology of Vela X is the result of an asymmetric RS interaction associated with expansion of the SNR into medium whose density is higher in the NE regions. The cocoon appears to result from the RS approaching and displacing the PWN from the NE, then wrapping around the highest-pressure regions of the nebula close to the pulsar, then finally coming together on the opposite side of the pulsar and over-pressuring the entrained plasma there.

There remain important considerations for which extension of our modeling to MHD will be necessary. In particular, since our HD simulations do not treat the evolution of the PWN magnetic field, our knowledge of the synchrotron losses suffered by particles in different regions of the PWN is quite incomplete. This, along with magnetic effects that might dominate the dynamics on some spatial scales, will be important to consider in future works in order to address the overall distribution of the emission observed in the GeV and TeV bands.

P.S. acknowledges partial support from NASA grants NNX09AP99G, GO1-12100X, and TM6-17002X, and NASA Contract NAS8-03060. In addition, he gives thanks to the Aspen Physics center, under whose hospitality portions of this work were completed. The authors thank Douglas Bock for providing the radio image shown in Figure 2, and Iurii Sushch for helpful discussions about the Vela SNR system. We also thank the anonymous referee for a careful review of the manuscript and for helpful suggestions that have improved the presentation of the work.

ORCID iDs

P. Slane https://orcid.org/0000-0002-6986-6756
S. L. Snowden https://orcid.org/0000-0002-5991-3096
T. Temim https://orcid.org/0000-0001-7380-3144
J. Blondin https://orcid.org/0000-0001-9691-6803
M. Miceli https://orcid.org/0000-0003-0876-8391
R. A. Chevalier https://orcid.org/0000-0002-9117-7244
J. P. Hughes https://orcid.org/0000-0002-8816-6800
D. J. Patnaude https://orcid.org/0000-0002-7507-8115

References

Abdo, A. A., Ackermann, M., Ajello, M., et al. 2010, ApJ, 713, 146
Aharonian, F., Akhperjanian, A. G., Bazer-Bachi, A. R., et al. 2006, A&A, 448, L43
Aschenbach, B., Egger, R., & Trümper, J. 1995, Natur, 373, 587
Blondin, J. M., Chevalier, R. A., & Frierson, D. M. 2001, ApJ, 563, 806
Bocchino, F., Maggio, A., & Sciortino, S. 1999, A&A, 342, 839
Bock, D. C.-J., Sault, R. J., Milne, D. K., & Green, A. J. 2002, in ASP Conf. Ser. 271, Neutron Stars in Supernova Remnants, ed. P. O. Slane & B. M. Gaensler (San Francisco, CA: ASP), 187
Bock, D. C.-J., Turtle, A. J., & Green, A. J. 1998, AJ, 116, 1886
Chevalier, R. A. 1982, ApJ, 258, 790
Chevalier, R. A., & Reynolds, S. P. 2011, ApJL, 740, L26
de Jager, O. C., Slane, P. O., & LaMassa, S. 2008, ApJL, 689, L125
Dodson, R., Legge, D., Reynolds, J. E., & McCulloch, P. M. 2003, ApJ, 596, 1137
Dubner, G. M., Green, A. J., Goss, W. M., Bock, D. C.-J., & Giacani, E. 1998, AJ, 116, 813
Espinoza, C. M., Lyne, A. G., & Stappers, B. W. 2017, MNRAS, 466, 147
Frail, D. A., Bietenholz, M. F., & Markwardt, C. B. 1997, ApJ, 475, 224
Helfand, D. J., Gotthelf, E. V., & Halpern, J. P. 2001, ApJ, 556, 380
Hinton, J. A., Funk, S., Parsons, R. D., & Ohm, S. 2011, ApJL, 743, L7
Katsuda, S., Mori, K., Petre, R., et al. 2011, PASJ, 63, S827
Kolb, C., Blondin, J., Slane, P., & Temim, T. 2017, ApJ, 844, 1
Kuntz, K. D., & Snowden, S. L. 2008, A&A, 478, 575
LaMassa, S. M., Slane, P. O., & de Jager, O. C. 2008, ApJL, 689, L121
Lyne, A. G., Pritchard, R. S., Graham-Smith, F., & Camilo, F. 1996, Natur, 381, 497
Mangano, V., Massaro, E., Bocchino, F., Mineo, T., & Cusumano, G. 2005, A&A, 436, 917
Markwardt, C. B., & Ögelman, H. 1995, Natur, 375, 40
Markwardt, C. B., & Ögelman, H. B. 1997, ApJL, 480, L13
Matzner, C. D., & McKee, C. F. 1999, ApJ, 510, 379
Miceli, M., Bocchino, F., Maggio, A., & Reale, F. 2005, A&A, 442, 513
Milne, D. K. 1968, AuJPh, 21, 201
Moriguchi, Y., Yamaguchi, N., Onishi, T., Mizuno, A., & Fukui, Y. 2001, PASJ, 53, 1025
Nichols, J. S., & Slavin, J. D. 2004, ApJ, 610, 285
Page, D. 2013, APS, 2013, J4.001
Pavlov, G. G., Teter, M. A., Kargaltsev, O., & Sanwal, D. 2003, ApJ, 591, 1157
Sankrit, R., Blair, W. P., & Raymond, J. C. 2003, ApJ, 589, 242
Slavin, J. D., Smith, R. K., Foster, A., et al. 2017, ApJ, 846, 77
Snowden, S. L., Mushotzky, R. F., Kuntz, K. D., & Davis, D. S. 2008, A&A, 478, 615
Sushch, I., & Hnatyk, B. 2014, A&A, 561, A139
Sushch, I., Hnatyk, B., & Neronov, A. 2011, A&A, 525, A154
Truelove, J. K., & McKee, C. F. 1999, ApJS, 120, 299
Tsunemi, H., Miyata, E., & Aschenbach, B. 1999, PASJ, 51, 711
White, R. L., & Long, K. S. 1991, ApJ, 373, 543
Wilms, J., Allen, A., & McCray, R. 2000, ApJ, 542, 914
Wongwathanarat, A., Hammer, N. J., & Müller, E. 2010, A&A, 514, A48
Yoshikoshi, T., Kifune, T., Dazeley, S. A., et al. 1997, ApJL, 487, L65